Modelling and Analysis of Spontaneous Brain Activity

Hlinka, Jaroslav
2010

Modelling and Analysis of Spontaneous Brain Activity

Post-Graduate Student:
ING. MGR. JAROSLAV HLINKA

Institute of Computer Science of the ASCR, v. v. i.
Pod Vodárenskou věží 2
182 07 Prague 8, CZ

hlinka@cs.cas.cz

Supervisor:
PROF. DOROTHEE AUER, PHD [1]
PROF. STEPHEN COOMBES, PHD [2]

[1] School of Clinical Sciences
[2] School of Mathematical Sciences
University of Nottingham
Nottingham, NG7 2RD, UK

stephen.coombes@nottingham.ac.uk

Field of Study:
Neuroimaging and Mathematical Neuroscience

The work was supported by the EC FP6 Marie Curie Action Programme (MEST-CT-2005-021170) and by the EC FP7 project BrainSync (EC: HEALTH-F2-2008-200728, CR: MSM/7E08027). I thank both my supervisors for long-term support in my work, Milan Paluš and Martin Vejmelka for valuable discussions of the nonlinearity/nongaussianity topic and Dante Mantini for providing fMRI data for the analysis reported in the second part of this paper.

Abstract

In brain imaging and neuroscience in general, the scientific and application interest in spontaneous brain activity has rapidly increased in the recent years. The key role of formalised models and effective data analysis methods for further development of the field is becoming widely accepted. In this paper we describe two applications of mathematics in the field. The first concerns modelling of the temporal properties of spontaneous brain activity fluctuations while the second assesses the potential of nonlinear analysis methods in the study of the commonly observed synchronisation patterns.

1. Introduction

The last two decades have witnessed great progress in mapping neural networks associated with task-induced brain activation using neuroimaging techniques – with functional magnetic resonance imaging (fMRI) playing a crucial role. More recently, identification of resting state networks (RSN) paved the way to investigation of spontaneous task-unrelated brain activity [1]. The first cardinal feature characterising RSN is low-frequency fluctuation (LFF, $0.01 - 0.1$Hz) of blood oxygenation level dependent (BOLD) fMRI signals synchronised between spatially distinct, but functionally connected brain areas. Specific patterns of this functional connectivity (FC) in terms of temporal synchronisation between remote neurophysiologic events are the second key feature of spontaneous brain activity.

In the first part of this paper we focus on modelling of LFF, following our study recently published in Physical Review Letters [2]. The second part deals with the potential of application of nonlinear analysis methods for FC – this work has recently been accepted to Neuroimage [3].

2. Candidate model for low-frequency fluctuation

The neuroscientific relevance of this fluctuation has been repeatedly confirmed by reports of its relation to electrophysiological measurements of brain activity [1]. Nevertheless, the role of these fluctuations as well as the underlying mechanism is still unclear. Current models of spontaneous brain activity have not yet fully addressed the question of the origin of low-frequency fluctuations. Typically, the recent modelling papers do mention LFF property of some version of the signal [4, 5], but the relation to and relevance for the neuroimaging signals is often vague. Further, all of the proposed mechanisms rely on long-range inter-regional interactions or advocate the necessary role of transmission delays and noise. In contrary, below we propose a local model of emergence of LFF not relying on particular delays and noise. For slightly more detail and colored version of the illustrations we refer the reader to our full paper [2], **available online** under Open Access.

2.1. Introduction

The principle of the proposed model lies in postulating a local feedback loop regulating the activity level based on previous memory of the localised system. As an example of such a regulatory process we have implemented a simple phenomenological model of the action of endogenous cannabinoids on synaptic activity. Indeed, other known regulatory mechanism could be also considered.

We document that the local network activity can show slow to ultra-slow fluctuations that do not have to match the timescale of the memory mechanism. Rather, they can exhibit arbitrarily slow frequencies dependent on other parameters of the model.

Endogenous cannabinoids (CBs) represent a fundamentally new class of *retrograde* messengers [6], which are released postsynaptically and bind to presynaptic CB receptors. One function of endogenous CBs is to regulate neurotransmitter release via activation of presynaptic CB receptors, allowing neurones to regulate, via feedback, their upstream neuronal inputs [7]. This suppression of upstream presynaptic release of GABA or glutamate is termed *depolarisation-induced suppression of inhibition* (DISI) or *depolarisation-induced suppression of excitation* (DISE) respectively [8, 9].

After introducing the full model, we first analyse the fast-scale behaviour of a synaptically coupled network of Morris-Lecar neurons and subsequently describe the emergence of nested fast and ultra-slow oscillations in the network when endowed with a phenomenological form of retrograde second messenger signalling that can support DISE. We hypothesise that when linked to other modules in a larger network the latter would be reflected as an ultra-slow component of the macroscopic network dynamics and could therefore underlie those seen in spontaneous brain activity (SBA).

2.2. Model description

2.2.1 Synaptically coupled network of Morris-Lecar neurons: For the single neuron we have chosen the Morris-Lecar (ML) [10] neuron model. This is a classical two dimensional conductance based model, often used as an idealized fast-spiking pyramidal neuron, written in the form

$$\dot{v} = f(v,w) + I + s(t), \qquad \dot{w} = g(v,w). \quad (1)$$

Here v plays the role of a voltage variable, w that of a gating variable, I is a fixed input and $s(t)$ represents a time varying synaptic input. The details of the functional forms for $f(v,w)$ and $g(v,w)$ can be found e.g. in [11] (with time measured in ms). The structure of the phase-plane and nullclines is recapitulated in Figure 1 for $s = 0$.

Indexing each neuron in the network with $i = 1, \ldots, N$ the synaptic drive to the i-th neuron is given by

$$s_i(t) = g_s(v_s - v(t)) \sum_{j=1}^{N} W_{ij} \sum_{m\in\mathbb{Z}} \eta(t - T_j^m), \quad (2)$$

where T_j^m is the m-th firing time of the j-th neuron, v_s the synaptic reversal potential and W_{ij} the connection strength between neurons i and j with a global conductance scaling g_s. The function $\eta(t)$ captures the shape of a conductance change in response to the arrival of an action potential. Here we choose an alpha function and write $\eta(t) = \alpha^2 t e^{-\alpha t} H(t)$, where H is a Heaviside step function. The firing times are specified in terms of a threshold h according to

$$T_i^m = \inf\{t \mid v_i(t) > h, \dot{v}_i > 0, t > T_i^{m-1}\}. \quad (3)$$

We focus on the case of an excitatory globally coupled network with homogeneous connectivity and therefore set $W_{ij} = 1/N$ and $v_s = 2 > 0$ with respect to the resting state.

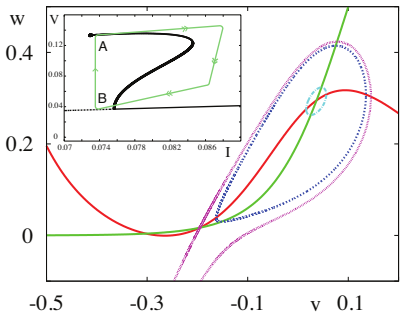

Figure 1: Phase-plane portrait for the Morris-Lecar model with constant external drive $I = 0.0761$. The voltage (gating) nullcline is in red (green). A large amplitude stable limit cycle (blue, dashed) coexists with a stable fixed point at $v \sim 0.04$. A small amplitude unstable orbit also exists (light blue, dash-dot). The separatrix (pink, stable manifold of saddle at $v \sim -0.2$) delimits the basin of attraction for the stable fixed point at $v \sim -0.3$. The associated bifurcation diagram illustrating bistability of the large amplitude limit cycle and the fixed point at $v \sim 0.04$ is shown in the inset. Here unstable orbits emerge in a Hopf bifurcation.

2.2.2 DISE mechanism: The endocannabinoid level is directly linked to the effective depolarisation, which we define by:

$$v_e(t) = \frac{1}{N} \sum_{j=1}^{N} \int_0^\infty K(t-s) v_j(s) ds, \quad (4)$$

where K is a temporal kernel reflecting the cannabinoid dynamics, $K(t) = 0$ for $t < 0$. Here we choose $K(t) = \lambda e^{-\lambda t} H(t)$, where λ^{-1} is an indirect measure of the long time-scale for cannabinoid dynamics, which is on the order of tens of seconds to minutes [9]. As a minimal model of DISE we assume that if the global CB level is sufficiently high then all excitatory synapses are blocked. In this case the network becomes uncoupled in the sense that excitatory synaptic currents drop to zero.

We implement this model of DISE by letting the firing threshold adjust in response to $v_e(t)$ according to

$$h = \begin{cases} v^{\text{th}} & v_e \leq v_e^{\text{th}} \\ \infty & v_e > v_e^{\text{th}} \end{cases}. \qquad (5)$$

The threshold v_e^{th} controls when the level of CB is sufficient to trigger DISE. In essence the model (5) means that synaptic interaction is curtailed if the effective level of depolarisation becomes too large.

2.3. Results

2.3.1 Model properties: Before we focus on the effects of DISE on the network dynamics, we analyse the fast-scale dynamics of the network. We first focus on the most symmetric oscillatory states expected to exist in a globally coupled system – namely the fully synchronous and asynchronous 'splay' (evenly distributed) solution. These are guaranteed by symmetry arguments [12].

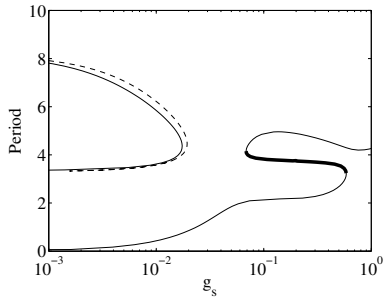

Figure 2: The period of the synchronous (solid line) and splay (dashed line) solutions as function of the coupling strength g_s. The numerically stable section of the synchronous solution branch for strong coupling is shown in thick line.

Synchronous solutions: In the synchronous state all neurons have identical T-periodic trajectories with firing times given by $T_i^m = mT$ for all i. In this case the synaptic drive to every neuron takes the identical form $s(t) = g_s(v_s - v(t))P(t)$, where $P(t) = \sum_{m\in\mathbb{Z}} \eta(t - mT)$ can be shown to equal to

$$P(t) = \frac{\alpha^2 e^{-\alpha t}}{1 - e^{-\alpha T}} \left[t + \frac{T e^{-\alpha T}}{1 - e^{-\alpha T}} \right], \qquad t \in [0, T), \qquad (6)$$

with $P(t)$ periodically extended outside $[0, T)$. Equation (1) may then be solved as a periodic boundary value problem (PBVP) for the periodic orbit $(v(t), w(t)) = (v(t + T), w(t + T))$ with $v(0) = v^{\text{th}}$. This describes the synchronous orbit given that the corresponding mean depolarisation does not trigger the DISE mechanism.

We solve this PBVP numerically, using XPPAUT [13]. The period of these solutions as a function of the coupling g_s is shown in Figure 2.

While these synchronous solutions must exist for small enough g_s, using a weakly coupled oscillator description with standard techniques reviewed in [14], we established that such solutions are unstable.

Splay solutions: For an asynchronous splay state the firing times are given by $T_j^m = mT + jT/N$. In the limit $N \to \infty$ network averages may be replaced by time averages due to:

$$\lim_{N\to\infty} \frac{1}{N} \sum_{j=1}^{N} F(jT/N) = \frac{1}{T} \int_0^T F(t)dt, \qquad (7)$$

for any T-periodic function $F(t) = F(t + T)$. Hence a splay state in which all neurons fire is given by $v_i(t) = v(t + iT/N)$, where $v(t)$ is a T-periodic solution of (1) with $s(t) = g_s(v_s - v(t))P_0$ and $P_0 = \int_0^T P(t)dt/T = 1/T$.

Solving the PBVP, we find that for small g_s the splay state has a similar period to that of the synchronous solution (see Figure 2). Note that for the splay state $v_e(t)$ takes on the constant value $v_0 = \int_0^T v(t)dt/T$. This is lower than the DISE threshold and therefore the DISE mechanism is not triggered. A weak-coupling analysis shows that the splay solution is also unstable.

Clustered solutions: While the instability of both the synchronous and splay solution for weak coupling can be determined semi-analytically, direct numerical simulations of the network suggest that another specific stable oscillatory solution exists even for the weak coupling. This has a hybrid form where the network splits into several clusters of fully synchronised neurons. These clusters then form a splay with evenly distributed phases.

Interestingly this type of solution typically further combines with a special type of clustered solution that can also occur for a wide range of g_s. This type of solution can be predicted purely from the theory. Consider two clusters of neurons; one in a (clustered) splay state, populating the orbit corresponding to the stable limit cycle of a single neuron; the other cluster consistsing of neurons sitting at rest at the central fixed point, which is stable for a sufficient level of synaptic input from the oscillating cluster of neurons. This can be described using

the differential-algebraic system

$$\dot{v} = f(v,w) + I + r\frac{g_s}{T}(v_s - v), \quad \dot{w} = g(v,w),$$
$$0 = f(\overline{v},\overline{w}) + I + r\frac{g_s}{T}(v_s - \overline{v}), \quad 0 = g(\overline{v},\overline{w}), \quad (8)$$

where r is the fraction of firing neurons and $(v(t + iT/M), w(t + iT/M))$ with $M = Nr$, and $(\overline{v},\overline{w})$ describe neurons in the splay and resting cluster respectively. In this case $v_e = rv_0 + (1-r)\overline{v}$.

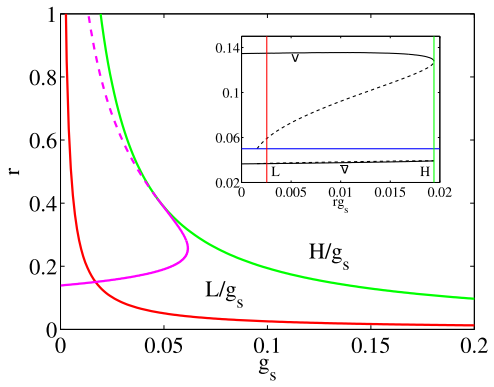

Figure 3: Fraction of firing neurons r as a function of the synaptic coupling strength g_s. See text for details.

For $v_e < v_e^{\text{th}}$ the parameter region of existence for such a solution is illustrated in the inset of Figure 3, where a pair of splay states (with $r \neq 1$) only coexists with a rest state for $rg_s \in [L, H]$. Here the splay state is annihilated in a saddle-node bifurcation at $rg_s = H$, while below $rg_s = L$ the central fixed point becomes unstable (assuming the oscillating cluster sitting at the upper branch of the limit cycle solution). For fixed rg_s, as g_s is increased, v_e grows until it reaches v_e^{th} and activates the DISE mechanism. The border in the (r, g_s) parameter plane where $v_e = v_e^{\text{th}}$ for a cluster state is shown in Figure 3 (magenta line), and we see that it defines a critical curve marking the onset of DISE which we can write in the form $g_s = g_c(r)$. In the absence of DISE, cluster states with limit cycle corresponding to the upper branch of the limit cycle solution would exist for a greater area of parameter space defined by the right-infinite strip between the lines L/g_s and H/G_s.

For $g_s < g_c(r)$ direct numerical simulations do indeed show cluster states with properties in excellent agreement with the solution of (8) (with $v(0) = v^{\text{th}}$) up to small fluctuations. An example is shown in Figure 4.

For a given value of g_s the fraction of neurons r in the firing state is a function of initial data, as expected. Importantly, after transients, the mean depolarisation signal is flat (no oscillations) and the period of oscillation of a firing neuron is of the same order of magnitude as a single isolated neuron.

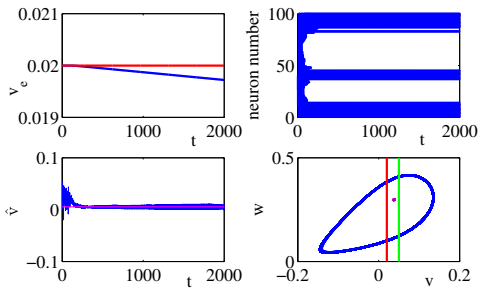

Figure 4: A cluster state for $N = 100$, $g = 0.03$, $v_e^{\text{th}} = 0.02$, $\lambda = 10^{-5}$. Top left: a plot of the average signal $v_e(t)$, showing that after transients the emergent state lies below the threshold to activate DISE (red line). Top right: A raster plot of spike times, illustrating the drop-out of some neurons and the emergence of a splay state with the fraction of firing neurons $r = 0.38$. Bottom left: The average network potential $\widehat{v} = \sum_{i=1}^{N} v_i/N$ oscillates around the predicted value $rv_0 + (1-r)\overline{v}$ (magenta line) for $r = 0.38$. Bottom right: Phase plane dynamics for the network (dropping transients) showing that the network has split into two clusters (one with a common periodic orbit shown in blue with a period $T \sim 6$ and a rest state in purple). $v^{\text{th}} = 0.05$ (green line), $v_e^{\text{th}} = 0.02$ (red line).

2.3.2 Emergence of LFF: In the region where $g_s > g_c(r)$ and DISE precludes the existence of the above discussed cluster state we expect more exotic non-periodic network states to emerge. Notably, while stable synchronous oscillations are possible with increasing g_s, the average depolarisation for these rhythms is relatively high and also an increasing function of g_s. Hence there is also a critical value of g_s at which the DISE mechanism will also preclude the existence of this periodic *synchronous* state.

The mechanism for LFF emergence for this stronger coupling is as follows. A synchronous (or near synchronous) solution can lead to a strong level of average depolarisation for which $v_e(t) > v_e^{\text{th}}$. This activates the DISE mechanism, precluding further synaptic input and subsequently leading to a drop in network firing activity and hence a drop in $v_e(t)$. Once $v_e(t)$ drops sufficiently to cross v_e^{th} from above then excitatory synaptic currents can once again drive the network leading to an increase in $v_e(t)$ so that the process may repeat over. In this case the emergent time scale of the network rhythm is set by the duration of $v_e(t)$ above v_e^{th}. Even for a synchronous solution this will depend on initial data, so that network oscillations would not generically be periodic.

To quantify the value of possible inter-spike intervals (ISIs) we focus on synchronous rhythms with

$(v(0), w(0)) = (v^{\text{th}}, w_0)$ for some given w_0 and solve the BVP $v_e(0) = v_e^{\text{th}} = v_e(\Delta)$ with $s(t) = g_s(v_s - v(t))P(t)$.

The growth of the ISI, Δ, as a function of g_s is shown in Figure 5, together with results from direct simulations. The numerical spread of ISIs for low g_s can be ascribed to fast multi-spike bursts. With higher g_s a single spike response is more common and the period of the network state is accurately predicted by the theory.

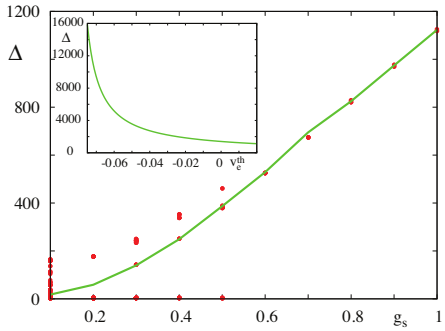

Figure 5: The predicted synchronous population ISI (in ms) as a function of g_s, for $w_0 = 0.121$ (green line), fits the ISIs seen in direct numerical simulations with $N = 100$ (red dots). Other parameters as in Figure 4. The inset shows the increase in ISI with decreasing v_e^{th} for $g_s = 1$.

Note that the spike times considered here are only those that contribute to synaptic currents, while the neurons do in fact spike on a fast time scale during the synaptically silent period. Hence, the network as a whole shows *nested* oscillations with a slow variation of synaptic currents superimposed on fast oscillations of the instantaneous average network voltage (see Figure 6 bottom left).

To understand how decreasing v_e^{th} can lead to a rapidly increasing Δ, as shown in the inset of Figure 5, it is useful to develop the correspondence of the evolution of the network (fixed parameters) with that of a single neuron with varying background drive I. Referring to the inset of Figure 1 the network can leave point A, corresponding to a synchronous firing state with average voltage v_2, when $v_e(t)$ drops below v_e^{th}. The subsequent large increase in synaptic drive causes a transition to the right of the saddle-node of periodics, where firing is not possible, and so synaptic currents fall which causes the transition to point B. This unstable fixed point, with voltage v_1, generates orbits which spiral outward for a time $T_1 = T_1(g_s)$ generating a signal with $v_e(t) > v_e^{\text{th}}$ (so that synaptic currents are suppressed). These transition to full blown nonlinear oscillations, with average voltage v_2 and $\dot{v}_e(t) < 0$, and complete the path to point A so that the process may repeat over. Making the convenient (and obviously not accurate) assumption that $v_{1,2}$ are constant then the BVP may be solved by hand for $\lambda = 0$ to give $\Delta = T_1(g_s)(v_1 - v_2)/(v_e^{\text{th}} - v_2)$, explaining the dependence of Δ on v_e^{th} seen in Figure 5.

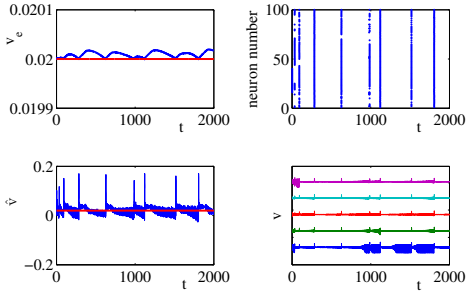

Figure 6: A similar plot to Figure 4 showing the emergence of slow synchronized firing patterns in the strong coupling regime with $g_s = 0.5$. Other parameters as in Figure 4. Bottom right shows voltage traces of 5 neurons (arbitrary offset for better display).

2.4. Discussion

Importantly, without any parameter fine-tuning, we see the emergence of very large ISIs for large values of g_s, which are largely independent of the network size. Moreover, in contrast to other network models of slow oscillations (< 1 Hz) [15] we do not require a mixture of excitation and inhibition. As shown in the inset of Figure 5 with decreasing choices of v_e^{th} can easily achieve ISIs on the order of tens of seconds. Thus DISE in the strong coupling regime is a candidate mechanism for the generation of ultra-slow rhythms.

3. Functional connectivity - analysing dependence patterns

3.1. Introduction

In functional neuroimaging, the most widely spread method of measuring functional connectivity between a pair of regions is computing a linear correlation of activity time series derived from these regions by e.g. simple spatial averaging across all the voxels in the regions. Linear correlation is also widely used to obtain so-called correlation maps by correlating the seed voxel or seed region signal with signal from all the other voxels in the brain, or constrained to gray matter area. From all possible bivariate measures of association, linear correlation is clearly a method of first choice, reflecting the assumption that the relationship between the fMRI time series can be suitably approximated by a multivariate Gaussian white noise process. Additionally, linear correlation is a well-known statistical concept, sufficiently simple to allow wide use and easy communication of results between researchers of diverse backgrounds.

On the other hand, from the mid-1980's, nonlinear approaches to analysis of brain signals are getting increased interest of researches who consider nonlinearity as an intrinsic property of brain dynamics, see e.g. [16] for a review. Hemodynamic nonlinearities are known to affect the blood oxygenation level-dependent (BOLD) fMRI signal [17]. More specifically, non-linearity of dependence between fMRI time series during resting state has been reported [18]. Use of non-linear measures of functional connectivity for the analysis of resting state data has been proposed [19], particularly including measures based on analysis of chaotic non-linear dynamical systems to analyze resting state data.

The question arises, to what extent and in what context is it justified and beneficial to use non-linear measures of functional connectivity. When linear correlation is used as a measure of functional connectivity, there are some implicit assumptions made. The first is that the information in the temporal order of the samples can be ignored (both within each timeseries and the mutual interaction). While the extent of justifiability of this assumption deserves exploration of its own, we keep this interim assumption for the purposes of this paper, not least in order to keep the comparison of linear correlation to nonlinear measures fair. Nonetheless, we ask if the instantaneous (zero-lag) dependence between the time series, expressed in the probability distribution p(X, Y), is fully captured by the linear correlation r(X,Y). We answer that this is true under the assumption of bivariate Gaussianity of the distribution. Bivariate normal distribution is fully characterised by its mean $\mu = (\mu_x, \mu_y)$ and its 2×2 covariance matrix $\mathrm{Cov}(X, Y)$ – if we allow for linear shifting and scaling, the remaining invariant parameter characterizing fully the distribution is indeed the correlation $r(X, Y)$. For a bivariate Gaussian distribution, the correlation also uniquely defines the mutual information shared between the two variables X, Y which can be computed as $I(X, Y) = I_{Gauss}(r) \equiv -\frac{1}{2}\log(1 - r^2)$.

On the other side, when the Gaussianity assumption does not hold, the distribution cannot be fully described by the mean and covariance. Interestingly, we can use the prominent properties of normal distribution to derive a useful lower bound on mutual information valid for a broad class of probability distributions. In particular, for a bivariate distribution $p(X, Y)$ with standard normal marginals $p(X)$, $p(Y)$, it holds that $I(X, Y) \geq I_{Gauss}(r) = -\frac{1}{2}\log(1 - r^2)$, where the equality holds exactly for bivariate Gaussian distributions. This allows us to quantify the deviation from Gaussianity as the difference between the total mutual information of the two variables $I(X, Y)$ and the mutual information $I_{Gauss}(r) = -\frac{1}{2}\log(1-r^2)$ that correspond to bivariate Gaussian distribution with the observed correlation r.

While there are many potential nonlinear FC measure candidates, mutual information holds a specific position among these for its generality. In theory, it is general enough to capture an arbitrary form of dependence relation between the variables without any apriori model restrictions on its form. The properties of mutual information allow us not only to test the suitability of linear correlation through probing the Gaussianity of the fMRI time series, but also to construct a quantitative estimate of connectivity information neglected by the use of linear correlation. This gives the amount of additional information available and bounds the potential contribution of non-linear alternatives over the Pearson correlation coefficient.

We implement the outlined ideas by comparing the total mutual information between the signals with the mutual information between the signals in surrogate datasets. These surrogates are generated in a way that preserves the linear correlation, but cancels any nonlinear information by enforcing bivariate Gaussian distribution on the surrogate signal-pair. This approach allows us to both test and quantify the deviation from Gaussianity, providing a principled guide in judging the suitability of linear correlation as a measure of FC. The focus on bivariate Gaussianity as the crucial condition of suitability of use of linear correlation as FC index, along with the illustrative quantitative estimation of the deviation from Gaussianity by means of the mutual information neglected by linear correlation, are the two main contributions of this study to the discussion of fMRI functional connectivity methods. We apply the presented method to parcel-average time series obtained from resting state fMRI BOLD signal of healthy subjects, testing and quantifying the deviation from bivariate Gaussianity.

3.2. Material and Methods

3.2.1 Data: Twelve right-handed healthy young volunteers (5 males and 7 females, age range 20 – 31 years) participated in the study. Each volunteer underwent two scanning runs of 10 minutes in a resting-state condition.

Scanning was performed with a 3T MR scanner (Achieva; Philips Medical Systems). Three hundred 3D-volumes with repetition time of 2 seconds, whole brain coverage and spatial resolution of $3 \times 3 \times 3$ mm^3 were used for the analysis. Standard preprocessing steps were applied, see our full paper [3] for details.

Ninety parcels from the Automated Anatomical Labeling (AAL) atlas were used to extract mean BOLD time series after masking out non-gray matter voxels. The anatomical positions of the parcels are described in [20]. Every parcel time series was orthogonalized with respect to motion parameters and global mean signal and high-pass filtered at 1/120Hz.

3.2.2 Analysis: As already mentioned in the Introduction, for a bivariate distribution $p(X,Y)$ with standard normal marginals $p(X)$, $p(Y)$, it holds that

$$I(X,Y) \geq I_{Gauss} = -\frac{1}{2}\log(1-r^2), \qquad (9)$$

where the equality holds exactly for bivariate Gaussian distributions. The inequality (9) stems from the fact, that normal distribution is the *maximum* entropy distribution for a given covariance matrix (or for a given correlation, as we assume without loss of generality that $\sigma(X) = \sigma(Y) = 1$). From the relation between mutual information and entropy ($I(X,Y) = H(X) + H(Y) - H(X,Y)$) it follows that mutual information of Gaussian distribution $I_{Gauss}(r)$ is then *minimal* from all distributions of given correlation r, under the assumption of fixed marginal entropies, which is true when the marginals have standard normal distribution. Note that the assumption of normality of the marginals is far less restrictive than it might seem. First, approximate data normality is commonly assumed in areas not restricted to fMRI FC analysis. More importantly, even if we find particular data deviating strongly from normality, any sample distribution can be monotonously transformed to match normal distribution.

To assure precise non-Gaussianity estimates, we have indeed carried out this 'normalization' step. It consists in assigning the appropriate percentile to each value of a given variable and then replacing the original values of the variable by values corresponding to these percentiles in a standard normal distribution. Note that this normalization step does not affect mutual information between the time series.

For two discrete random variables X_1, X_2 with sets of values Ξ_1 and Ξ_2, the mutual information is defined as

$$I(X_1,X_2) = \sum_{x_1\in\Xi_1}\sum_{x_2\in\Xi_2} p(x_1,x_2)\log\frac{p(x_1,x_2)}{p(x_1)p(x_2)},$$

where the probability distribution function is defined by $p(x_i) = Pr\{X_i = x_i\}, x_i \in \Xi_i$ and the joint probability distribution function is $p(x_1,x_2)$ is defined analogously. When the discrete variables X_1, X_2 are obtained from continuous variables on a continuous probability space, then the mutual information depends on a partition ξ chosen to discretize the space. Here a simple box-counting algorithm based on marginal equiquantization method [21] was used, i.e., a partition was generated adaptively in one dimension (for each variable) so that the marginal bins become equiprobable. This means that there is approximately the same number of data points in each marginal bin. In this paper we used a simple pragmatic choice of $Q = 8$ bins for each marginal variable.

For each session, we have computed the mutual information (MI) for each pair of parcels, yielding a symmetric 90-by-90 matrix of MI values. To minimize bias of the MI estimates due to inevitable discretization and finite sample estimation, the MI values were further monotonously transformed to correct for these effects. This transformation map was generated using random samples from normal distributions with correlation ranging from 0 to 1 in 200 steps of 0.005. For each correlation value, 50000 such random bivariate samples with N=300 independent observations each were generated and the mean of their MI as computed by the equiquantization method was tabulated. As for bivariate Gaussian random distribution with correlation r the true MI is $I_{Gauss} = -\frac{1}{2}\log(1-r^2)$, this tabulation allows approximate transformation of estimated MI to true bivariate MI.

To compare the (total) mutual information to the portion of information conveyed in the linear correlation, for each dataset, 99 random realizations of multivariate time series preserving the linear structure but canceling the nonlinear structure were constructed, and MI was computed for these surrogates. If the original time series dependence structure was Gaussian (and therefore fully captured by the linear correlation), the MI in the surrogates should not differ from the original MI, up to some random error.

The surrogates were constructed as multivariate Fourier transform (FT) surrogates [22]: realizations of multivariate linear stochastic process which mimic individual spectra of the original time series as well as their cross-spectrum. The multivariate FT surrogates are obtained by computing the Fourier transform of the series, keeping unchanged the magnitudes of the Fourier coefficients (the amplitude spectrum), but adding the same random number to the phases of coefficients of the same frequency bin; the inverse FT into the time domain is then performed.

The idea of comparing the MI of data to MI of 'linear' surrogates rather than directly to linear correlation of data has two aspects. First, it allows a direct quantitative comparison of the nonlinear and linear connecti-

vity, while correlation and mutual information estimators have generally different properties. Second, generation of the surrogates allows direct statistical testing of the difference. However, this procedure generates 99 estimates of the linear MI for each parcel pair; one for each surrogate. While these are useful for hypothesis testing, for general presentation of the difference we use the mean value of these 99 values. In the following we refer to this as 'Gaussian' MI, and it actually closely estimates the MI of a bivariate Gaussian distribution $I_{Gauss}(r) = -\frac{1}{2}\log(1-r^2)$, where r stands for the correlation of the two variables. The 'neglected' MI is estimated by the difference between data MI and the Gaussian MI: $I_{neglected}(X,Y) = I(X,Y) - I_{Gauss}(r)$.

3.2.3 Statistical tests: For each session and each parcel pair, non-Gaussianity was tested at $p = 0.05$ by comparing data MI against MI distribution of multivariate FT surrogates. To correct for mutual comparisons, the number of significant pairs in given session was than tested against the null hypothesis that the number of individual significant entries has a binomial distribution $B(n = 4005, p = 0.05)$, where $n = 4005 = \frac{90(90-1)}{2}$ is the number of all parcel pairs and $p = 0.05$ is the single entry false positive rate under condition of pure Gaussianity of the bivariate distributions.

As it may be argued that the assumption of pair independence is too lenient, but the exact level of dependence is difficult to establish, we also carried out group level tests. The percentages of significant pairs were compared by means of a paired t-test to the percentages of significant pairs obtained from 'shadow' datasets. Each shadow dataset was created as a multivariate FT surrogate of normalized data of a given session, preserving only the linear structure of the dataset after normalisation of univariate marginals. Subsequently, each shadow dataset has undergone the same procedure as original data, including the initial normalization, generation of multivariate surrogates, computation of MI and statistical testing of pair-wise MI against surrogates. In this way, we have mimicked the full procedure using the shadow dataset, accounting for any potential bias in the detection rate introduced by numerical properties of the algorithm. Apart from the percentages, we have also tested the mean neglected information from data versus shadow datasets by mean of a paired t-test.

3.3. Results

3.3.1 Descriptive assessment: In descriptive terms, the data MI has proved very similar to the Gaussian MI (see Figure 7). In particular, averaging across all parcel pairs, the data MI ranged between 0.04-0.10 bits for different sessions, while the neglected MI was more than an order of magnitude smaller (0.0005-0.0068 bits). Nevertheless, the neglected MI was consistently positive, which was not the case for shadow datasets (ranging from -0.0007 to 0.0016 bits).

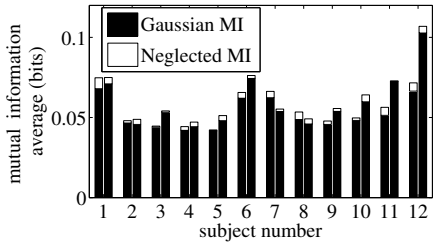

Figure 7: Comparison of the average Gaussian and neglected information. Each stackbar represents values for one session, averaged across all parcel pairs.

Independently of the strength of coupling, the data MI was moreover typically within the range of surrogate MI, as illustrated on Figure 8 top. Although the session

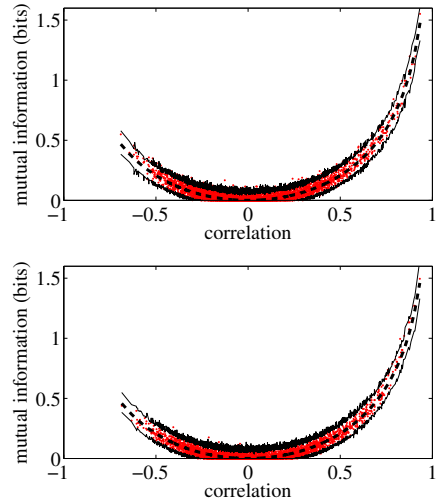

Figure 8: Mutual information as function of correlation in an example dataset (top) and the corresponding linearized 'shadow' dataset. Each dot corresponds to MI of one parcel pair; full lines show the 1st and 99th percentile of the surrogate distribution; dashed line shows the theoretical prediction for Gaussian data. The session with the most non-Gaussianity is depicted.

with the most non-Gaussianity is depicted here, the distribution of computed MI for data and the corresponding shadow dataset (Figure 9 bottom) are almost indiscernible. Also, apart from the random error due to MI estimation from short time series, which is shared by data and shadow data, both scatters follow well the theoretical prediction of dependence of MI on linear correlation ($I_{Gauss} = -\frac{1}{2}\log(1-r^2)$, valid exactly under Gaussianity).

3.3.2 Statistical tests: The percentage of parcel pairs with significant non-Gaussianity was slightly elevated in all sessions above the 5% expected under the null hypothesis (ranging from 5.3 to 10.0% of significant pairs in different sessions). If all the parcel pairs were considered independent this would constitute significant percentage for all but 5 of the sessions considered. Group level tests confirmed the statistical deviation from Gaussianity – when compared on group level by means of a paired t-test, the counts of pairs with significant nonlinearity were significantly higher than similar counts obtained from shadow datasets ($t = 6.26, \mathrm{df} = 23, p < 0.00001$). Also, the neglected information in data averaged over parcel pairs was positive for all sessions and on average had value 0.0029 bits. On the other side, the neglected information in the shadow datasets fluctuated around zero with mean of 0.0006 bits. This difference was also clearly statistically significant ($t = 6.51, \mathrm{df} = 23, p < 0.00001$).

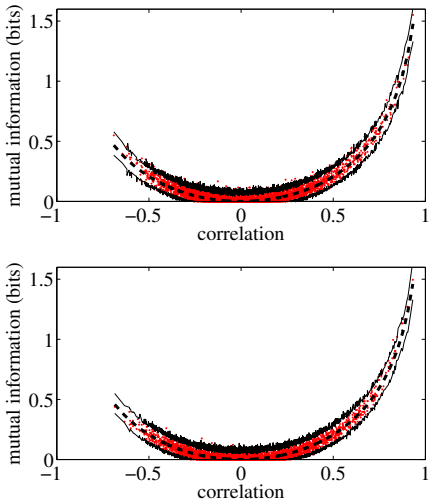

Figure 9: Mutual information as function of correlation in an example dataset (top) and the corresponding linearized 'shadow' dataset. Each dot corresponds to MI of one parcel pair; full lines show the 1st and 99th percentile of the surrogate distribution; dashed line shows the theoretical prediction for Gaussian data. The session with the most non-Gaussianity is depicted.

3.4. Discussion

The presented study confirms the suitability of linear correlation as functional connectivity measure for fMRI time series by testing and quantifying the deviation from bivariate Gaussianity using mutual information. The quantitative assessment revealed that the portion of mutual information neglected by using linear correlation instead of considering an arbitrary non-linear form of instantaneous dependence is minor. Nevertheless, formal group-level test revealed that the percentage of parcel-pairs with significant non-Gaussian dependence contribution is indeed above random. Overall we conclude that practical relevance of nonlinear methods trying to improve over linear correlation might be limited by the fact that the data are indeed almost Gaussian.

It is important to keep in mind that the observed deviations from Gaussianity might not reflect only a stationary non-Gaussianity in neuronal connectivity. In the presented framework, deviation from the null hypothesis could be caused also by nonstationarity of the signal.

For completeness, we note that linearity is also often discussed as an alternative to nonlinear, potentially chaotic deterministic dynamical systems. In this context caution is warranted with the interpretation of many 'chaotic' characteristics such as fractional correlation dimension or Lyapunov exponents when the underlying system might be of stochastic (non)linear nature rather than deterministic (non)linear dynamical system, and particularly when short time series such as those acquired from fMRI are being analyzed.

4. Summary

In this paper, we have described two exemplar contributions of mathematical modelling and analysis to the study of large-scale spatiotemporal patterns of spontaneous brain activity. This investigation inevitably led to new questions.

Challenges in spontaneous brain activity modelling

Further investigation is needed to reveal the role of regulatory feedbacks in the slow brain activity dynamics. The search should not be limited to the action of endocannabinoids that served as an example carrier of this mechanism in this paper - the role of other neuromodulators or metabolic fatigue should be investigated.

Nongaussianity in fMRI functional connectivity

The confirmation of suitability of linear correlation as a functional connectivity measure for resting state fMRI provides important support to the common practice in neuroimaging. Nevertheless, the scope of possible generalisation of the results remains an open question. Particularly interesting is the generalisation to time-lagged dependence structures and other preprocessing and time series extraction methods. Explicit modelling might have something to say regarding the emergence of largely 'linear' or 'gaussian' dependencies on the macroscopic level of regional fMRI signals from the highly nonlinear nature of the local neuronal dynamics.

Most of the questions discussed above are not only interesting intellectual challenges – the answers are crucial for further development and applications of the study of spontaneous brain activity.

References

[1] M.D. Fox and M.E. Raichle, "Spontaneous fluctuations in brain activity observed with functional magnetic resonance imaging," *Nature Reviews Neuroscience*, vol. 8, no. 9, pp. 700–711, 2007.

[2] J. Hlinka and S. Coombes, "Depolarization Induced Suppression of Excitation and the Emergence of Ultraslow Rhythms in Neural Networks," *Physical Review Letters*, vol. 104, no. 6, 2010.

[3] J. Hlinka, M. Palus, M. Vejmelka, D. Mantini, and M. Corbetta, "Non-gaussian dependence and neglected information in resting fmri functional connectivity," *NeuroImage*, In Press.

[4] C.J. Honey, R. Kotter, M. Breakspear, and O. Sporns, "Network structure of cerebral cortex shapes functional connectivity on multiple time scales," *Proceedings of the National Academy of Sciences of the United States of America*, vol. 104, no. 24, pp. 10240–10245, 2007.

[5] G. Deco, V. Jirsa, A.R. McIntosh, O. Sporns, and R. Koetter, "Key role of coupling, delay, and noise in resting brain fluctuations," *Proceedings of the National Academy of Sciences of the United States of America*, vol. 106, no. 25, pp. 10302–10307, 2009.

[6] T. Freund, I. Katona, and D. Piomelli, "Role of endogenous cannabinoids in synaptic signaling," *Physiological Reviews*, vol. 83, no. 3, pp. 1017–1066, 2003.

[7] R. Wilson and R. Nicoll, "Neuroscience - Endocannabinoid signaling in the brain," *Science*, vol. 296, no. 5568, pp. 678–682, 2002.

[8] T. Ohno-Shosaku, T. Maejima, and M. Kano, "Endogenous cannabinoids mediate retrograde signals from depolarized postsynaptic neurons to presynaptic terminals," *Neuron*, vol. 29, no. 3, pp. 729–738, 2001.

[9] A. Straiker and K. Mackie, "Depolarization-induced suppression of excitation in murine autaptic hippocampal neurones," *Journal of Physiology*, vol. 569, no. 2, pp. 501–517, 2005.

[10] C. Morris and H. Lecar, "Voltage oscillations in the barnacle giant muscle-fiber," *Biophysical Journal*, vol. 35, no. 1, pp. 193–213, 1981.

[11] S. Han, C. Kurrer, and Y. Kuramoto, "Dephasing and bursting in coupled neural oscillators," *Physical Review Letters*, vol. 75, no. 17, pp. 3190–3193, 1995.

[12] P. Ashwin and J.W. Swift, "The dynamics of n-weakly coupled identical oscillators," *Journal of Nonlinear Science*, vol. 2, no. 1, pp. 69–108, 1992.

[13] B. Ermentrout, *Simulating, Analyzing, and Animating Dynamical Systems: A Guide To Xppaut for Researchers and Students*. Philadelphia, PA, USA: Society for Industrial and Applied Mathematics, 2002.

[14] F.C. Hoppensteadt and E.M. Izhikevich, *Weakly connected neural networks*. Secaucus, NJ, USA: Springer-Verlag New York, Inc., 1997.

[15] A. Compte, M. Sanchez-Vives, D. McCormick, and X. Wang, "Cellular and network mechanisms of slow oscillatory activity (¡ 1 Hz) and wave propagations in a cortical network model," *Journal of Neurophysiology*, vol. 89, no. 5, pp. 2707–2725, 2003.

[16] C. Stam, "Nonlinear dynamical analysis of EEG and MEG: Review of an emerging field," *Clinical Neurophysiology*, vol. 116, no. 10, pp. 2266–2301, 2005.

[17] J.A. de Zwart, P. van Gelderen, J.M. Jansma, M. Fukunaga, M. Bianciardi, and J.H. Duyn, "Hemodynamic nonlinearities affect BOLD fMRI response timing and amplitude," *NeuroImage*, vol. 47, no. 4, pp. 1649 – 1658, 2009.

[18] P.J. Lahaye, J.B. Poline, G. Flandin, S. Dodel, and L. Garnero, "Functional connectivity: studying nonlinear, delayed interactions between BOLD signals," *NeuroImage*, vol. 20, no. 2, pp. 962–974, 2003.

[19] X.P. Xie, Z.T. Cao, and X.C. Weng, "Spatiotemporal nonlinearity in resting-state fMRI of the human brain," *NeuroImage*, vol. 40, no. 4, pp. 1672–1685, 2008.

[20] N. Tzourio-Mazoyer, B. Landeau, D. Papathanassiou, F. Crivello, O. Etard, N. Delcroix, B. Mazoyer, and M. Joliot, "Automated anatomical labeling of activations in SPM using a macroscopic anatomical parcellation of the MNI MRI single-subject brain," *NeuroImage*, vol. 15, no. 1, pp. 273–289, 2002.

[21] M. Palus, V. Albrecht, and I. Dvorak, "Information theoretic test for nonlinearity in time series," *Physics Letters A*, vol. 175, no. 3-4, pp. 203–209, 1993.

[22] D. Prichard and J. Theiler, "Generating surrogate data for time series with several simultaneously measured variables," *Physical Review Letters*, vol. 73, no. 7, p. 951, 1994.